Journal of Intelligent & Robotic Systems (2022) 106: 22
https://doi.org/10.1007/s10846-022-01611-6

REGULAR PAPER

Scale Force Control of an Exoskeleton for Human Performance Augmentation

Lin Lang [1,2] · Junhao Xiao [1] · Yunshu Sun [3] · Huimin Lu [1] · Zongtan Zhou [1] · Chunbaixue Yang [2]

Received: 29 August 2021 / Accepted: 7 March 2022 / Published online: 6 September 2022

Abstract

Exoskeletons for human performance augmentation have been widely applied in many environments, ranging from military, industry, to construction. For load-carrying augmentation exoskeletons, one of the key issues is to control the human-robot interaction (HRI) force. This paper firstly proposes a unified framework for scale force control (SFC) of human-bearing augmentation exoskeleton (HBAE) and robot-bearing augmentation exoskeleton (RBAE). Furthermore, a mid-level SFC method was proposed, in the light of both cognitive and physical HRIs (cHRI and pHRI). On this basis, a hybrid low-level controller was designed for load-carrying exoskeletons (LCEs). Finally, the proposed method was simulated on an LCE. The simulation results demonstrate the effectiveness of our SFC approach: the pilot is always provided with an arbitrary scaled-down interaction force, regardless of the load state.

Keywords Scale force control (SFC) · Augmentation exoskeleton · Load-carrying exoskeleton (LCE) · Hybrid control

1 Introduction

Non-medical exoskeletons are wearable devices that augment the physical capabilities of able-bodied users [1]. These augmentation exoskeletons can be applied to various scenarios, namely, lifting heavy objects in factories, carrying weapons in the military, clearing obstacles during rescue operations, and handling package, to name but a few. By contrast, medical exoskeletons, [2] also known as orthotics, assist patients with limb pathologies [3], or old people with limited mobility and strength.

Both augmentation and medical exoskeletons have been studied for sixty years, starting with Hardiman's prototype in the late 1960s [4]. During the past decade, significant advancement has been achieved on both types of exoskeletons. The technology of medical exoskeletons is relatively mature. Representative products, such as ReWalk [5], Hybrid Assistive Limb (HAL) [6], and Ekso [7], have already been applied in the real world. Meanwhile, augmentation exoskeletons are still under development. The relatively advanced prototypes of augmentation exoskeletons, such as Berkeley lower extremity exoskeleton (BLEEX) [8], Human Universal Load Carrier (HULC) [9], Sarcos XOS 2 [2], body extender (BE) [10], etc., enable pilots to carry heavy loads or lift bulky objects. However, their user experience is not ideal. Sometimes, the pilots need to expend more energy, and their movements might be hindered [11]. Motion hinderance, and other practical problems like shaking and instability, may arise from hardware and control strategy.

The hardware of augmentation exoskeletons faces key issues like power supply, mechanical design, lightweight actuators, and transmission efficiency [12]. The control strategy relating to safe and comfortable human-robot interaction (HRI) is as important as hardware. As a human-in-loop robot system, augmentation exoskeletons involve both cognitive HRI (cHRI) and physical HRI (pHRI) [13]. An augmentation exoskeleton needs to follow the motivation of its pilot. In return, the pilot needs to know the specific state of the robot system. On the human side, cHRI makes the pilot aware of the robot and its operating state, and helps the wearer control the entire system. Coupled with cHRI, pHRI often manifests as

✉ Junhao Xiao
junhao.xiao@ieee.org

[1] National University of Defense Technology, Changsha 410072, China

[2] Hunan University of Finance and Economics, Changsha 410000, China

[3] CNNP Liaoning Nuclear Power Co., Ltd., Changsha, China

force or torque signals, exerting a direct impact on assistance effect and wearable comfort [14]. Both HRIs can be used as the input of a controller. But it is more difficult to acquire and process cHRI signals, e.g., surface electromyography (sEMG), than pHRI signals. Currently, control strategies based on pHRI signals tend to be more reliable than those based on cHRI signals.

Much work has been done on the control strategy of augmentation exoskeleton. The reduction of resistive forces is one of the research hotspots. Hong M.B. et al. [15] and Kim J. et al. [16] designed linkage mechanisms to pinpoint the rotation axes of the exoskeleton's ankle and knee joints, and those of the corresponding human joints. Their mechanisms can reduce discomfort kinematically. Walsh C.J. et al. [17, 18] developed a lightweight exoskeleton for the leg to reduce the load on the muscles of wearers. Despite their effectiveness, lightweight exoskeletons a may not sufficiently reduce resistive forces. Zero-resistance exoskeleton control could be realized based on the key technique of detecting the wearer's movement intention. In fact, it is possible to estimate the movement intention from the inverse dynamics of exoskeletons, and from the interactive forces directly measured by force/torque sensors [19, 20]. Nevertheless, the estimated movement intention has an inherent delay compared to the real movement intention. In addition, impedance control has been employed in several approaches [21, 22]. Proper impedance of the exoskeleton potentially reduces the HRI forces. Yet it is hard to estimate an accurate impedance for natural movements.

The past few years has witnessed the emergence of many pHRI-based controllers. Tucker summed up these controllers, and presented a generalized framework of the human-exoskeleton system [1]. Under the framework, there is a three-level hierarchical robot: the high-level estimates movement intention, the mid-level layer generates the desired target, and the low-level eliminates error. Specific control laws are realized in the latter two levels. To date, few designers have paid attention to pHRI-based mid-level controllers. In general, the desired control target is simply set as zero interaction force or a predefined trajectory. On the contrary, the design of low-level controllers is relatively mature [23]. By the usage of pHRI information, low-level controllers can be classified into indirect force control and direct force control.

Indirect force control includes position tracking control and impedance control. Based on backstepping, Chen S. et al. [24, 25]designed a robust multi-input multi-output (MIMO) adaptive controller for a hydraulic exoskeleton. The controller can precisely track the desired trajectory, which is generated from pHRI force and pHRI model, and simultaneously tackle unknown modelling parameters and uncertainties. Li Z. et al. [26] put forward an adaptive fuzzy controller, which enables an upper-limb exoskeleton to track the predefined curve, and to tolerate various uncertainties. Lee S and Sankai Y., Yang Z. et al., Tran H.T. et al., and Aguirre-Ollinger G. et al. [27–30] relied on impedance control to improve the HRI dynamics, and significantly smooth the interaction force.

Direct force control encompasses force/torque feedback control and observer-based force control. Force/torque feedback control directly utilizes the interaction force/torque measured by sensors [31], while the observer-based force control derives the interaction force/torque with the inverse model of the exoskeleton and a filter, eliminating the need of force/torque sensors [32].

Along with the design of the low-level controller, significant work has been devoted to issues like disturbance estimation [26, 33], compensation for modelling error [25, 34], and tolerance of nonlinear parameter uncertainty [24, 35]. Nonetheless, the control of augmentation exoskeletons is way different from the control of conventional manipulators. Human experience should be highlighted, and the human side does not need excessively high control accuracy. Almost all the methods above neglect the transformation of cHRI from load and robot side to human side, a critical issue in the control of every human-in-loop system.

This paper makes two major contributions: Firstly, a unified scale force control (SFC) framework was developed for both human- and robot-bearing augmentation exoskeletons. The framework, consisting of a mid-level force controller, and a low-level hybrid controller, provides an arbitrary scaled-down HRI force, regardless of the load state. Secondly, an SFC method was put forward under the SFC framework, giving consideration to the two-way transformation of cHRI and pHRI. A scale factor was defined as the assistance coefficient, which allows for real-time modulation. Since pHRI and cHRI are theoretically coupled in the human-robot system, the SFC not only reduces the wearer's effort in load bearing, but also feeds back the load-side information to the human side via pHRI.

The remainder of this paper is organized as follows: Section 2 presents the concept of SFC for augmentation exoskeletons, and verifies the method on an elbow joint exoskeleton; Section 3 introduces the designed load-carrying exoskeleton (LCE), builds its dynamic model, and designs a hybrid controller; Section 4 simulates the LCE, and analyzes the results; Section 5 summarizes the findings, discuses the limitations, and looks forward to future work.

2 SFC

2.1 Concept of SFC

The concept of SFC arises from the control of teleoperation with force feedback. Figure 1 compares the components and

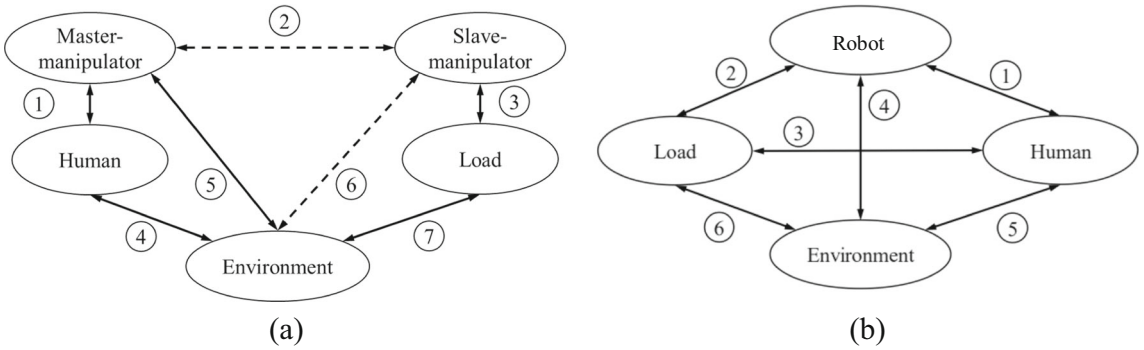

Fig. 1 Components and their interactions in teleoperation system (a) and augmentation exoskeleton (b) Note: Solid and dashed lines represent physical and information interactions, respectively

their interactions of teleoperation system (a) and those of augmentation exoskeleton (b). It can be observed that the two systems have nearly identical interactions between components. The main difference between them is that: In the augmentation exoskeleton, the robot serves both as the master-manipulator and slave-manipulator in the teleoperation system, and the load can interact directly with human; in the teleoperation system, the load-side information is scaled down, before being transferred to the human side via interaction ②. The SFC of the augmentation exoskeleton can be understood as a way to enable the human to operate the load, or use only a part of the force/torque, which is equal to the scaled-down load force/torque of the teleoperation system. The scale factor is the ratio of human force/torque to load force/torque.

To find a preferable control target for SFC, it is firstly necessary to classify the augmentation exoskeleton. As shown in Fig. 1(b), the augmentation exoskeleton consists of four mutually interactive components: human, robot, environment, and load. Note that the load is no longer regarded as a part of the robot or the environment, because the system control needs to achieve two targets: load bearing, and intention following. The environment usually refers to the ground or obstacles. In some situations, the two-way interactions ④, ⑤ and ⑥ may be absent; in most cases, interactions ② and ③ will not occur simultaneously.

According to the object that directly interacts the load, the augmentation exoskeleton can be divided into two classes: human-bearing augmentation exoskeleton (HBAE), and robot-bearing augmentation exoskeleton (RBAE). In the HBAE, the human directly contacts the load via interaction ③, and the human limbs are supported by the robot via interaction ①. The typical prototypes of HBAE include cable driven arm exoskeleton (CAREX) [36] and KIT-EXO-1 [37]. In the RBAE, the robot directly contacts the load via interaction ②, under the guidance of the pilot. The representative devices of RBAE are cable-actuated dexterous exoskeleton for neurorehabilitation (CADEN)-7 [38], and BLEEX [8].

2.2 Control Target Selection

2.2.1 HBAE

The defining feature of the HBAE is the direct human operation of the load. In general, the HBAE system requires the pilot to have flexible limbs and acute sensations. Figure 2(a) illustrates a single elbow joint HBAE: the human limb is bound with a robot limb, and the pHRI torque T_p and load torque T_l are measurable or estimable. To design a mid-level controller, the potential control targets need to be evaluated in four aspects: assistance, following, anti-disturbance, and informing.

i. Assistance: The main function of the augmentation exoskeleton is to provide aid. An exoskeleton must be able to undertake most loads in the task, such as carrying loads, lifting heavy objects, and handling materials.
ii. Following: In any no-load condition, the exoskeleton must follow the pilot's movements without any hinderance. The pilot should not expend more energy than he/she does without wearing the exoskeleton.
iii. Anti-disturbance: Anti-disturbance is required for security reasons. An augmentation exoskeleton is comparable to a power amplifier. If disturbance signals are regarded as the source signals and amplified, it may harm the human side or cause damage to the load side. Apart from the disturbances from the external environment, the term "disturbance" also include undesired motions on the human side, e.g., trembling, and unconditioned reflexes.
iv. Informing: Informing specifically refers to force informing, rather than visual informing or other approaches. The human-robot system involves two controllers: the human brain and the exoskeleton computer. Both controllers require the original or scaled load-side information to accomplish the task.

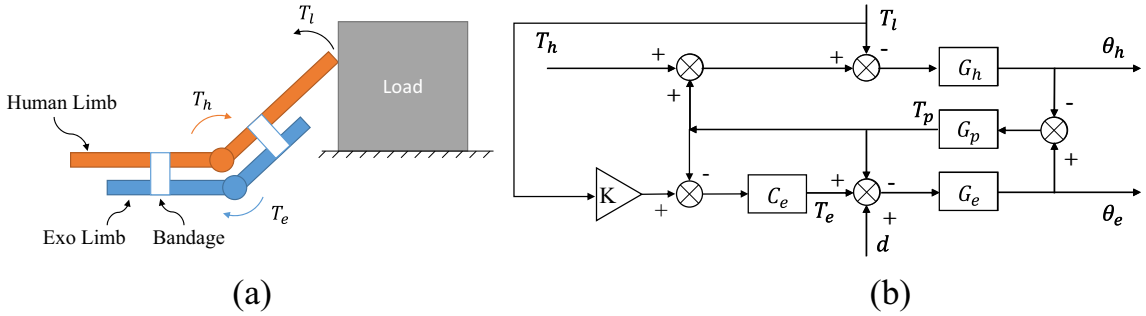

Fig. 2 A single elbow joint HBAE (a) and its control diagram with the control targe $T_p = K \cdot T_l$ (b) Note: C_e is the robot controller; K is the scale factor; d is the external disturbances; G_h, G_p, and G_e are the models of human, interaction, and robot, respectively

The potential control targets are listed in Table 1. It can be inferred that all five targets can pass load-side information to the human side, thanks to the direct interaction between human and load. However, zero interaction force control is not suitable for HBAE, for the exoskeleton cannot assist the pilot under this control mode. Neither is the target $T_e = K \cdot T_p$ applicable: the control will fail, if T_e and T_p have a definite relation. As for targets $T_e = K \cdot T_h$ and $T_p = K \cdot T_h$, neither could effectively handle human-side disturbances. Thus, advisable control target is $T_p = K \cdot T_l$, which handles all the above issues excellently. The control diagram with the target $T_p = K \cdot T_l$ is presented in Fig. 2(b). The following is a detailed analysis on the single elbow joint HBAE in Fig. 2(a) with the control target $T_p = K \cdot T_l$ $(0 < K < 1)$:

When the system reaches a steady state, the wearer's effort can be obtained as:

$$T_h = (1-K) \cdot T_l \tag{1}$$

Eq. (1) implies that the target has the capacity for assistance. During the following movements, the load torque T_l becomes zero, such that the interaction torque $T_p = K \cdot 0 = 0$. In this case, the robot does not interfere with the wearer's motion. The progress information always exists, for the wearer directly contacts the load. Next, the anti-disturbance property is analyzed against the control diagram in Fig. 2(b). Without loss of generality, the dynamics equations of the system can be established as:

$$T_h + T_p - T_l = m_h\ddot{\theta}_h + b_h\dot{\theta}_h \tag{2}$$

$$T_e - T_p + d = m_e\ddot{\theta}_e + b_e\dot{\theta}_e \tag{3}$$

$$T_p = b_p\left(\dot{\theta}_e - \dot{\theta}_h\right) + k_p(\theta_e - \theta_h) \tag{4}$$

where, m_h and m_e are inertia coefficients; b_h and b_e are damping coefficients; b_p and k_p are parameters of the interaction model. The low-level controller of the exoskeleton can be designed as a proportional-integral (PI) controller:

$$\begin{aligned} T_e(s) &= \left(K \cdot T_l(s) - T_p(s)\right)C_e(s) \\ &= \left(K \cdot T_l(s) - T_p(s)\right)\left(K_c + \frac{K_i}{s}\right) \end{aligned} \tag{5}$$

where, K_c and K_i are controller parameters; s is the Laplace operator. Taking the Laplace transform of Eqs. (2)–(4) and eliminating variables $\theta_e(s)$ and $\theta_h(s)$:

$$\begin{aligned} \frac{T_p(s)}{b_p s + k_p} &= \frac{1}{m_h s^2 + b_h s}\left(T_h(s) + T_p(s) - T_l(s)\right) \\ &\quad + \frac{1}{m_e s^2 + b_e s}\left(T_e(s) - T_p(s) + d(s)\right) \end{aligned} \tag{6}$$

Substituting Eq. (5) into Eq. (6), the system equation from the inputs $T_h(s)$, $T_l(s)$, and $d(s)$ to the output $T_p(s)$ can be obtained as:

$$\begin{aligned} &\left(\frac{1}{b_p s + k_p} + \frac{1}{m_h s^2 + b_h s}\right)T_h(s) + \left(\frac{K(K_c s + K_i)}{m_e s^3 + b_e s^2} - \frac{1}{m_h s^2 + b_h s}\right)T_l(s) + \frac{1}{m_e s^2 + b_e s}d(s) \\ &= \left(\frac{1}{b_p s + k_p} - \frac{1}{m_h s^2 + b_h s} + \frac{K_c s + K_i}{m_e s^3 + b_e s^2}\right)T_p(s) \end{aligned} \tag{7}$$

The load task is achieved by the wearer's effort T_h and the robot's power T_p. From Eq. (7) and the final value theorem, the steady-state gain can be obtained as:

$$\left.\frac{T_p(s)}{T_h(s)}\right|_{s\to 0} = 0, \quad \left.\frac{T_p(s)}{d(s)}\right|_{s\to 0} = 0, \quad \left.\frac{T_p(s)}{T_l(s)}\right|_{s\to 0} = 0 \tag{8}$$

Table 1 Potential control targets of HBAE and their effects

Control target	As	F	Ad	I
T_p=0	N	Y	Y	Y
T_e=K·T_p, K>1	N	Y	Y	Y
T_e=K·T_h, K>1	Y	Y	N	Y
T_p=K·T_h, K>1	Y	Y	N	Y
T_p=K·T_l, 0<K<1	Y	Y	Y	Y

Note: **As, F**, **Ad**, and **I** are short for assistance, following, anti-disturbance, and informing, respectively; Y and N means a control target can or cannot execute the corresponding function well, respectively. The same below.

From Eq. (8), it can be concluded that the disturbances d and limb shaking ΔT_h will not be amplified by the exoskeleton. Even if they are transformed to the load side as ΔT_l, the system will not amplify the disturbances, when $0 < K < 1$.

2.2.2 RBAE

RBAE systems are much more diverse than HBAE systems. Compared with HBAE, RBAE provides a superior cHRI effect in the HRI system. Owing to the strength advantage of mechanical structure, RBAE can bear more loads and offer a wider range of assistance than HBAE. Fig. 3(a) illustrates a single elbow joint RBAE. It can be observed that, when the limb is extended, the load will be pushed to the right. In contrast with HBAE, RBAE contacts the load directly, and the human can only sense the load indirectly via interaction force T_p. The mid-level controller of RBAE is designed in the light of all four properties: assistance, following, anti-disturbance, and informing.

The potential control targets of the single elbow joint RBAE are listed in Table 2. In RBAE, load and pilot are separated by the robot, making it impossible for zero interaction force control to transfer load-side information to the human side. Neither control target $T_e = K \cdot T_p$ nor $T_e = K \cdot T_h$ can effectively handle human-side disturbances: the disturbances d are enlarged K times as a result of output through T_e, which is quite dangerous. The target $T_p = K \cdot T_h$ is not suitable for RBAE, because it intends to promote human movement without considering the loads. The advisable control target is still $T_p = K \cdot T_l$, the same as that for HBAE. The control diagram of RBAE with the target $T_p = K \cdot T_l$ is presented in Fig. 3(b). The following is a detailed analysis on the single elbow joint RBAE in Fig. 2(a) with the control target $T_p = K \cdot T_l\,(0 < K < 1)$:

Without considering disturbances d, when the system reaches a steady state, the wearer's effort can be obtained as:

$$T_h = T_p = K \cdot T_l \tag{9}$$

Eq. (9) indicates the assistance capacity of the target. The following movement situation is the same as HBAE. After the robot enters the swing phase, the load torque T_l becomes zero, and the interaction torque $T_p = K \cdot 0 = 0$ under the robot control. The load-side states will be partially transformed to the human side via the interaction torque T_p. Next, the anti-disturbance property is analyzed against the control diagram in Fig. 3(b). Without loss of generality, the dynamics equations of the system can be established as:

Table 2 Potential control targets of RBAE and their effects

Control target	As	F	Ad	I
T_p=0	Y	Y	Y	N
T_e=$K\cdot T_p$, K>1	Y	Y	N	Y
T_e=$K\cdot T_h$, K>1	Y	Y	N	Y
T_p=$K\cdot T_h$, K>1	Y	Y	N	N
T_e=$K\cdot T_l$, 0<K<1	Y	Y	Y	Y

$$T_h - T_p + d = m_h\ddot{\theta}_h + b_h\dot{\theta}_h \tag{10}$$

$$T_e + T_p - T_l = m_e\ddot{\theta}_e + b_e\dot{\theta}_e \tag{11}$$

$$T_p = b_p\left(\dot{\theta}_e - \dot{\theta}_h\right) + k_p(\theta_e - \theta_h) \tag{12}$$

where, m_h and m_e are inertia coefficients; b_h and b_e are damping coefficients; b_p and k_p are parameters of the interaction model. The low-level controller of the exoskeleton can be designed as a PI controller:

$$\begin{aligned} T_e(s) &= \left(K \cdot T_l(s) - T_p(s)\right)C_e(s) \\ &= \left(K \cdot T_l(s) - T_p(s)\right)\left(K_c + \frac{K_i}{s}\right) \end{aligned} \tag{13}$$

where, K_c and K_i are controller parameters; s is the Laplace operator. Taking the Laplace transform of Eqs. (10)–(12) and eliminating variables $\theta_e(s)$ and $\theta_h(s)$:

$$\begin{aligned} T_p(s) = &\frac{1}{m_h s^2 + b_h s}\left(T_h(s) - T_p(s) + d(s)\right) \\ &+ \frac{1}{m_e s^2 + b_e s}\left(T_e(s) + T_p(s) - T_l(s)\right) \end{aligned} \tag{14}$$

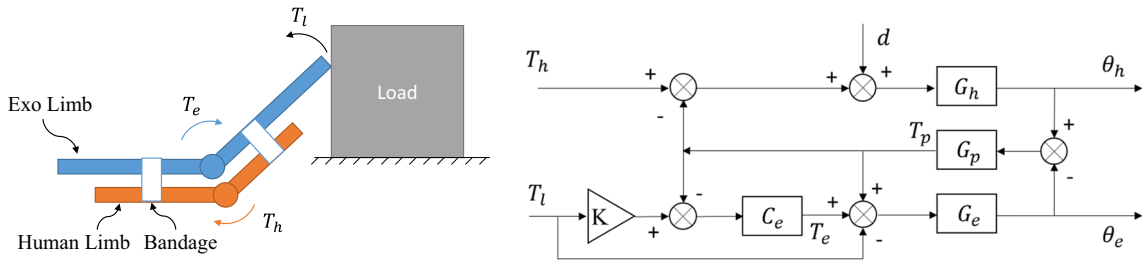

Fig. 3 A single elbow joint RBAE (a) and its control diagram with the control targe $T_p = K \cdot T_l$ (b)

Substituting Eq. (13) into Eq. (14), the system equation from the inputs $T_h(s)$, $T_l(s)$, and $d(s)$ to the output $T_e(s)$ can be obtained as:

$$K \cdot T_l(s) - \frac{T_h(s) + d(s)}{(m_h s^2 + b_h s) \cdot A} = \frac{s T_e(s)}{K_c s + K_i} - \frac{T_e(s)}{m_e s^2 + b_e s} \quad (15)$$

where, $A = \frac{1}{b_p s + k_p} + \frac{1}{m_h s^2 + b_h s} + \frac{1}{m_e s^2 + b_e s}$.

The load task is achieved by the wearer's effort T_p and the robot's power T_e. From Eq. (15) and the final value theorem, the steady-state gain can be obtained as:

$$\left.\frac{T_e(s)}{T_h(s)}\right|_{s\to 0} = 0, \quad \left.\frac{T_e(s)}{d(s)}\right|_{s\to 0} = 0, \quad \left.\frac{T_e(s)}{T_l(s)}\right|_{s\to 0} = 1 - \left(1 - \frac{b_e}{b_h}\right) K \quad (16)$$

The exoskeleton design needs to minimize the damping b_e. In the low-level controller, the damping torque can be estimated and compensated for. Thus, the value $\frac{b_e}{=} b_h$ is nearly zero.

From Eq. (16) and $\frac{b_e}{=} b_h \approx 0$, it can be concluded that the disturbances d and limb shaking ΔT_h will not be amplified by the exoskeleton. Even if they are transformed to the load side as ΔT_l, the system will not amplify the disturbances, when $0 < 1 - K < 1$.

2.3 Model of Multi-Body Exoskeleton

Multi-body exoskeleton is similar to a bipedal walking robot. The difference is that the movements are ultimately decided by the pilot, and the main task is not maintaining body balance.

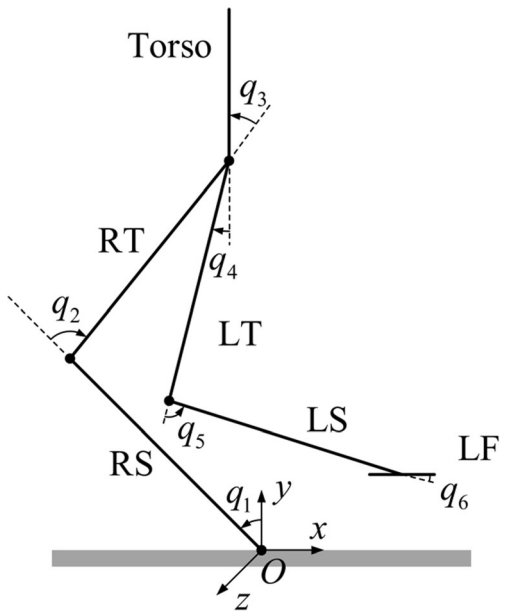

Fig. 4 Simplified diagram of multi-body exoskeleton and its coordinates. Note: R and L are right and left, respectively; S, T, and F are shank, thigh, and foot, respectively

Taking the supporting foot instead of the torso as the base coordinate, the case of right leg support is illustrated in Fig. 4. The model of left leg support can be obtained by analogy.

The human-robot back interaction point $\boldsymbol{p}$, the load-robot interaction point $\boldsymbol{l}$, and the human-robot swing leg interaction point $\boldsymbol{f}$ can be respectively expressed as:

$\boldsymbol{p} = [p_x p_y p_{rz}]^T$, $\boldsymbol{l} = [l_x l_y l_{rz}]^T$, $\boldsymbol{f} = [f_x f_y f_{rz}]^T$ (17).

where, p_x, p_y, l_x, l_y, f_x, and f_y are positions in base coordinate O_{xyz}; p_{rz} and l_{rz} are the pitch angles of the torso; f_{rz} is the pitch angle of the left foot. The velocities of the points can be described as:

$$\begin{aligned}\dot{p} &= \left[\dot{p_x}\ \dot{p_y}\ \dot{p_{rz}}\right]^T = \left[J_p(q)^{3\times 3} \quad 0^{3\times 3}\right]\dot{q} = J_p(q)\dot{q_r}\dot{l} \\ &= \left[\dot{l_x}\ \dot{l_y}\ \dot{l_{rz}}\right]^T = \left[J_l(q)^{3\times 3} \quad 0^{3\times 3}\right]\dot{q} = J_l(q)\dot{q_r}\dot{f} \\ &= \left[\dot{f_x}\ \dot{f_y}\ \dot{f_{rz}}\right]^T = \left[J_f(q)^{3\times 3} \quad 0^{3\times 3}\right]\dot{q} = J_f(q)\dot{q_r} \end{aligned} \quad (18)$$

where, $\boldsymbol{J_p(q)}$, $\boldsymbol{J_l(q)}$, and $\boldsymbol{J_f(q)}$ are Jacobian matrices; $\boldsymbol{q} = [q_1 q_2 q_3 q_4 q_5 q_6]^T$; $\boldsymbol{q_r} = [q_1 q_2 q_3]^T$.

The system dynamics can be described as:

$$\begin{aligned}&\boldsymbol{M(q)} \cdot \ddot{\boldsymbol{q}} + \boldsymbol{C}\left(\boldsymbol{q}, \dot{\boldsymbol{q}}\right) \cdot \dot{\boldsymbol{q}} + \boldsymbol{G(q)} \\ &= \boldsymbol{T_a} + \begin{bmatrix} \boldsymbol{J_l}^T(\boldsymbol{q}) \cdot \boldsymbol{F_l} \\ \boldsymbol{0}^{3\times 1} \end{bmatrix} + \begin{bmatrix} \boldsymbol{J_p}^T(\boldsymbol{q}) \cdot \boldsymbol{F_p} \\ \boldsymbol{0}^{3\times 1} \end{bmatrix} + \boldsymbol{J_f}^T(\boldsymbol{q}) \\ &\quad \cdot \boldsymbol{F_f} \end{aligned} \quad (19)$$

where, $\boldsymbol{M(q)} \in \mathbb{R}^{6\times 6}$ is a symmetric positive definite inertia matrix; $\boldsymbol{C}\left(\boldsymbol{q}, \dot{\boldsymbol{q}}\right) \in \mathbb{R}^{6\times 6}$ is the Coriolis and centrifugal matrix; $\boldsymbol{G(q)} \in \mathbb{R}^{6\times 1}$ is the gravity term; $\boldsymbol{T_a} \in \mathbb{R}^{6\times 1}$ is the actuator's torque; $\boldsymbol{F_p} \in \mathbb{R}^{3\times 1}$ is the back interaction force from human to robot; $\boldsymbol{F_l} \in \mathbb{R}^{3\times 1}$ is the back interaction force from load to robot; $\boldsymbol{F_f} \in \mathbb{R}^{3\times 1}$ is the foot interaction force from human to robot.

Since most of the loads are carried by the supporting leg of the exoskeleton, the controllers of the supporting leg and swing leg are designed separately. The system dynamics Eq. (19) can be decoupled as:

$$\begin{aligned}&\begin{bmatrix} M_1(q) & M_2(q) \\ M_3(q) & M_4(q) \end{bmatrix}\begin{bmatrix} \ddot{q}_r \\ \ddot{q}_l \end{bmatrix} + \begin{bmatrix} C_1\left(q, \dot{q}\right) & C_2\left(q, \dot{q}\right) \\ C_3\left(q, \dot{q}\right) & C_4\left(q, \dot{q}\right) \end{bmatrix}\begin{bmatrix} \dot{q}_r \\ \dot{q}_l \end{bmatrix} + \begin{bmatrix} G_r(q) \\ G_l(q) \end{bmatrix} \\ &= \begin{bmatrix} \tau_{ar} \\ \tau_{al} \end{bmatrix} + \begin{bmatrix} J_l{}^T(q) \cdot F_l \\ 0^{3\times 1} \end{bmatrix} + \begin{bmatrix} J_p{}^T(q) \cdot F_p \\ 0^{3\times 1} \end{bmatrix} + \begin{bmatrix} \tau_{fr} \\ \tau_{fl} \end{bmatrix} \end{aligned} \quad (20)$$

where, $\boldsymbol{q_l} = [q_4 q_5 q_6]^T$. The dynamics of the supporting leg can be sorted out as:

$$\boldsymbol{M_1(q)} \cdot \ddot{\boldsymbol{q}}_r + \boldsymbol{C_1}\left(\boldsymbol{q}, \dot{\boldsymbol{q}}\right) \cdot \dot{\boldsymbol{q}}_r = \boldsymbol{\tau_{ar}} + \boldsymbol{J_l}^T(\boldsymbol{q}) \cdot \boldsymbol{F_l} + \boldsymbol{J_p}^T(\boldsymbol{q}) \cdot \boldsymbol{F_p} + \boldsymbol{\omega} \quad (21)$$

where,

$$\boldsymbol{\omega} = -\boldsymbol{M_2}(\boldsymbol{q}) \cdot \ddot{\boldsymbol{q}}_l - \boldsymbol{C_2}\left(\boldsymbol{q}, \dot{\boldsymbol{q}}\right) \cdot \dot{\boldsymbol{q}}_l + \boldsymbol{\tau}_{fr} \tag{22}$$

$\boldsymbol{\omega}$ can be regarded as disturbances from the swing leg.

Most scholars agree that the physical HRI model is highly nonlinear and changeable with respect to different wearers and activities [39, 40]. Here, it is assumed that the foot pHRIs of the above multi-body exoskeleton are tightly combined, and the back pHRI model can be simplified as a spring damping model:

$$\boldsymbol{F}_p = \boldsymbol{k}_p \Delta \boldsymbol{r}_{he} + \boldsymbol{b}_p \Delta \dot{\boldsymbol{r}}_{he} \tag{23}$$

where, $\boldsymbol{k_p} = diag\ (k_{px}, k_{py}, k_{prz})$ is stiffness; $\boldsymbol{b_p} = diag\ (b_{px}, b_{py}, b_{prz})$ is damping; $\Delta \boldsymbol{r_{he}} \in \mathbb{R}^{3 \times 1}$ is the position deviation between human and robot.

Transforming the state variables from joint space $\boldsymbol{q}_r$ to workspace $\boldsymbol{r}_e$:

$$\begin{cases} \dot{\boldsymbol{r}}_e = \boldsymbol{J}_p(\boldsymbol{q})\dot{\boldsymbol{q}}_r \\ \ddot{\boldsymbol{r}}_e = \boldsymbol{J}_p(\boldsymbol{q})\ddot{\boldsymbol{q}}_r + \dot{\boldsymbol{J}}_p\left(\boldsymbol{q}, \dot{\boldsymbol{q}}\right)\dot{\boldsymbol{q}} \end{cases} \Rightarrow \begin{cases} \dot{\boldsymbol{q}}_r = \boldsymbol{J}_p^{-1}(\boldsymbol{q})\dot{\boldsymbol{r}}_e \\ \ddot{\boldsymbol{q}}_r = \boldsymbol{J}_p^{-1}(\boldsymbol{q})\ddot{\boldsymbol{r}}_e - \dot{\boldsymbol{J}}_p\left(\boldsymbol{q}, \dot{\boldsymbol{q}}\right)\dot{\boldsymbol{r}}_e \end{cases} \tag{24}$$

The dynamics Eq. (21) can be written as:

$$\begin{aligned} &\boldsymbol{A}(\boldsymbol{q})\ddot{\boldsymbol{r}}_e + \boldsymbol{B}\left(\boldsymbol{q}, \dot{\boldsymbol{q}}\right)\dot{\boldsymbol{r}}_e + \boldsymbol{G}_r(\boldsymbol{q}) \\ &= \boldsymbol{\tau}_{ar} + \boldsymbol{J}_l^T(\boldsymbol{q})\boldsymbol{F}_l + \boldsymbol{J}_p^T(\boldsymbol{q})\boldsymbol{F}_p + \boldsymbol{w} \end{aligned} \tag{25}$$

where,

$$\begin{aligned} \boldsymbol{A}(\boldsymbol{q}) &= \boldsymbol{M_1}(\boldsymbol{q})\boldsymbol{J}_p^{-1}(\boldsymbol{q}) \\ \boldsymbol{B}\left(\boldsymbol{q}, \dot{\boldsymbol{q}}\right) &= \boldsymbol{C_1}\left(\boldsymbol{q}, \dot{\boldsymbol{q}}\right)\boldsymbol{J}_p^{-1}(\boldsymbol{q}) - \boldsymbol{A}(\boldsymbol{q})\dot{\boldsymbol{J}}_p\left(\boldsymbol{q}, \dot{\boldsymbol{q}}\right)\boldsymbol{J}_p^{-1}(\boldsymbol{q}) \end{aligned} \tag{26}$$

According to the proposed pHRI model, the relationship between desired interaction force $\boldsymbol{F_d}$ and desired workspace position $\boldsymbol{r_{ed}}$ can be expressed as:

$$\boldsymbol{F_d} = \boldsymbol{k_p}(\boldsymbol{r_h} - \boldsymbol{r_{ed}}) + \boldsymbol{b_p}\left(\dot{\boldsymbol{r}}_h - \dot{\boldsymbol{r}}_{ed}\right) \tag{27}$$

Combined with Eq. (23), the deviation of interaction force can be expressed as:

$$\Delta \boldsymbol{F} = \boldsymbol{F_p} - \boldsymbol{F_d} = \boldsymbol{k_p}(\boldsymbol{r_{ed}} - \boldsymbol{r_e}) + \boldsymbol{b_p}\left(\dot{\boldsymbol{r}}_{ed} - \dot{\boldsymbol{r}}_e\right) \tag{28}$$

Thus, the desired workspace position $\boldsymbol{r_{ed}}$ can be obtained as:

$$\boldsymbol{r_{ed}}(t) = \boldsymbol{r}(t) + \boldsymbol{b_p}^{-1} e^{-\boldsymbol{k_p}\boldsymbol{b_p}^{-1}t} * \Delta \boldsymbol{F}(t) \tag{29}$$

where, $*$ is the convolution operation. The discrete form of $\boldsymbol{r_{ed}}$ can be defined as:

$$\begin{aligned} \boldsymbol{r_{ed}}(n) = \boldsymbol{r_e}(n) &+ \frac{T\Delta \boldsymbol{F}}{T\boldsymbol{k_p} + \boldsymbol{b_p}} \\ &+ \frac{\boldsymbol{b_p}}{T\boldsymbol{k_p} + \boldsymbol{b_p}}[\boldsymbol{r_{ed}}(n-1) - \boldsymbol{r_e}(n-1)] \end{aligned} \tag{30}$$

where. $n \in \mathbb{Z}, n \geq 1$; $\boldsymbol{r_e}(0) = \boldsymbol{0}; \boldsymbol{r_{ed}}(0) = \boldsymbol{0}$.

The model of multi-body exoskeleton lays the basis for the design of our hybrid controller.

2.4 Verification of SFC

To verify its feasibility, the proposed SFC method was tested on an elbow joint RBAE (Fig. 5). The test devices are as follows: a Gyems RMD-X brushless direct current (DC) torque motor, integrated with a field-oriented control (FOC) driver and an 18-bit absolute encoder; a one-dimensional (1D) force sensor for pHRI force measurement; a controller card based on ARM Cortex-M4 stm32f417; an embedded microprocessor that communicates with the motor through a controller area network (CAN) bus.

The dynamics of the single elbow joint RBAE can be expressed as

$$I_r \cdot \ddot{\theta} + f\left(\dot{\theta}\right) + G(\theta) = \tau_a + \tau_p + \tau_l \tag{31}$$

where $I_r$is the rotational inertia of the robot arm; θ is the joint angle between the robot link and horizontal direction; $f\left(\dot{\theta}\right)$ is the damping term; G is the gravity term; τ_a is the actuator's torque; τ_p is the HRI torque;τ_l is the load torque. Note that the load block is not considered as a part of the robot arm. The load torque τ_l can be estimated by:

$$\tau_l = MgLcos(\theta) + I_l \cdot \ddot{\theta} \tag{32}$$

where, M is the mass of the load; L is the distance between load center and rotation center; I_l is the rotational inertia of the load. The system parameters are given in Table 3. The control diagram is the same as Fig. 3(b). For simplicity, a PI controller with gravity compensation and velocity feedback is chosen as the low-level controller:

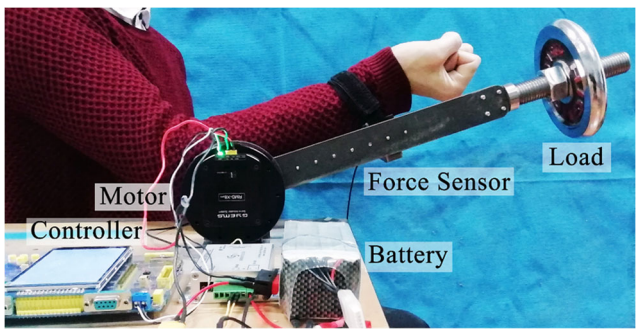

Fig. 5 Single elbow joint RBAE

Table 3 Parameters of the single elbow joint RBAE

Symbol	Definition	Value
m	Robot arm mass	1.10 kg
M	Load mass	1.41 kg
l	Robot arm mass center	0.18 m
L	Load mass center	0.34 m
r	Arm of interaction force	0.17 m

$$\tau_a = k_p r\left(f_p - f_{pd}\right) + k_i \int_0^t \left(f_p - f_{pd}\right) dt - k_d \dot{\theta} + G(\theta) \qquad (33)$$

where, $k_p = 300$, $k_d = 30$, and $k_i = 1$. The damping term $-k_d\dot{\theta}$ is used to improve the dynamic response of the system. According to the SFC concept, the desired interaction force $f_{pd} = K \cdot \tau_l$ with scale factor $K = 0.2$.

The experimental results are recorded in Fig. 6. As shown in Fig. 6(a), the robot arm followed the wearer's voluntary movement. As shown in Fig. 6(b), during the movement, the system generally tracked the desired force, with the maximum error staying below 0.45 N. As shown in Fig. 6(c), the joint torque fell within [−5.5 Nm, −2.5 Nm]. As shown in Fig. 6(d), the actual scale factor approximated the desired value $K = 0.2$, despite a slight fluctuation. This means the exoskeleton reduced the wearer's effort needed to carry the load block by one-fifth. The above results demonstrate the feasibility of the SFC, which allows the pilot to carry the same load with a scaled-down force, and enables he/she to perceive the target better. The scale factor K not only reduces the force needed to lift the heavy object, but also scales the mass of the object and transmits it to the wearer, creating a two-way feedback path between human and robot. In addition, the good coupling between cHRI and pHRI in the interaction system, so that the overall performance of the HRI system can be boosted by human experience.

3 SCF of LCE

Since there are more applications for RBAE than HBAE, the LCE, a typical RBAE for military uses, was selected for SFC. A novel LCE structure was devised with as few human-machine connections as possible. The loosely-coupled LCE was designed in the combined simulation environment of MATLAB and OpenSim. The source codes were uploaded to https://github.com/MoranHansir. The authors proposed a hybrid low-level controller to achieve the SFC target $T_p = K \cdot T_l$.

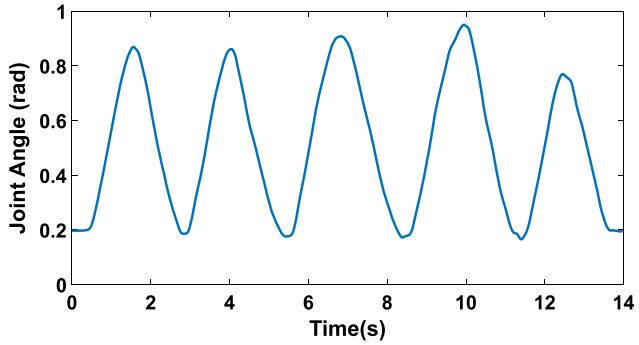

(a)

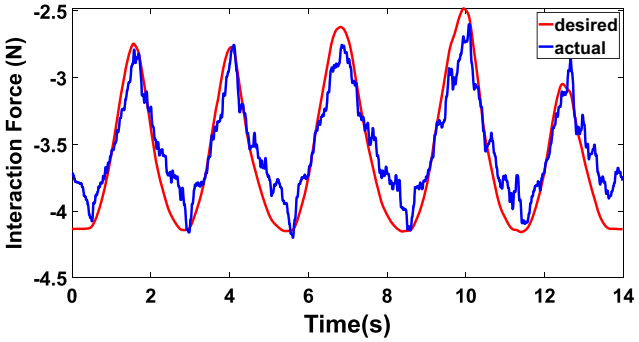

(b)

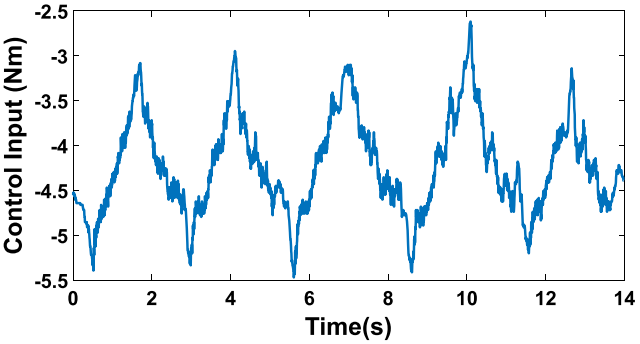

(c)

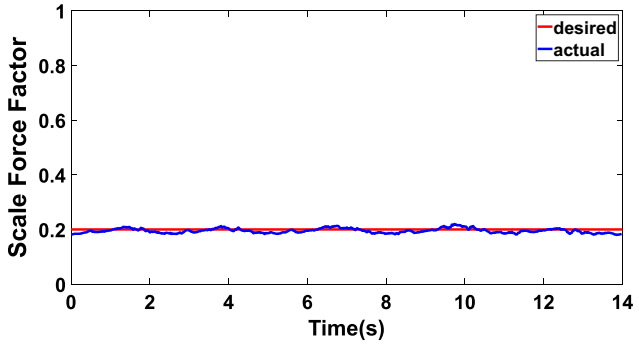

(d)

Fig. 6 Robot arm following pilot motions (a), tracking results of interaction force (b), actuator's control value (c), and result of SFC (d)

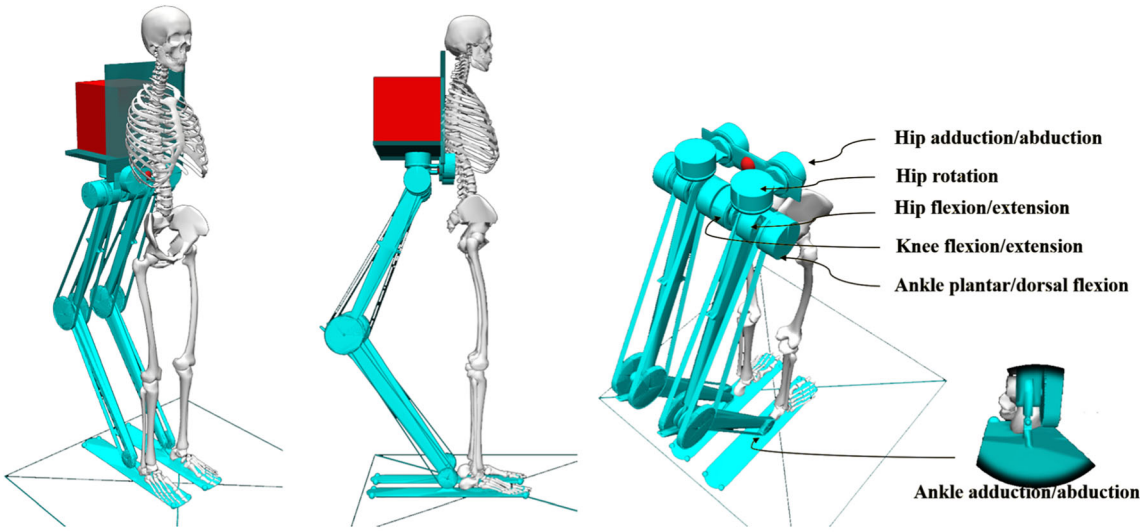

Fig. 7 Loosely-coupled LCE built by (a) Loosely-coupled load-carrying exoskeleton built by the Simbody dynamic engine, and the location of actuators and the corresponding DOFs (b). Note: The red box represents load

3.1 Loosely Coupled LCE

Figure 7 illustrates the designed LCE structure. The exoskeleton only connects with the wearer at the foot and back. The knee joint bends to the opposite direction of the wearer. Such a structure helps avoid human-robot interference. The relatively long exoskeleton limbs can adapt to pilot stature. In total, there are six degrees of freedom (DOFs), including four powered degrees (hip adduction/abduction, hip flexion/extension, knee flexion/extension, and ankle plantar/dorsal flexion), and two passive joints (hip rotation, and ankle adduction/abduction). As shown in Fig. 7(b), all powered actuators are near the waist. The knee and ankle joint torques are transmitted through cables.

To apply SFC $T_p = K \cdot T_l$ on the designed LCE, human-robot and load-robot interaction forces must be measured. Thus, a multidimensional force sensor was mounted on the back of the robot, and between the back of the pilot and robot. The exoskeleton footplate is two times larger than the normal human foot, primarily for increasing the stability region of the zero-moment point. To minimize the impact of the exoskeleton on normal human gait, only the pilot's forefoot is connected with the footplate.

3.2 Hybrid Controller Design

This work mainly investigates the SFC of the supporting leg. Following the SFC method in Section 2.2.2, the mid-level layer controller can be designed as:

$$\boldsymbol{F_p} = \boldsymbol{K} \cdot \boldsymbol{F_l} \tag{34}$$

where, $\boldsymbol{K} = diag\ (K_x, K_y, K_{rz})$ is the scale factor. The factors of the three DOFs K_x, K_y, and K_{rz}, all of which fall within [0, 1), can be chosen separately. Then, a hybrid low-level controller was devised to improve the effect of dynamic scale force tracking. The control block is illustrated in Fig. 8.

Note: The dotted block represents the hybrid controller, which combines the proportional term of the direct interaction force F_p and the inverse dynamic controller; $\hat{r}_{ed}^{1}$, $\hat{r}_{ed}^{2}$, and $\hat{\dot{r}}_{ed}^{2}$ are desired trajectories obtained using two tracking differentiators (TDs): TD-I and TD-II.

Drawing on Jinqing H. and Lulin Y. [41], TD-I and TD-II can be expressed as:

$$\begin{cases} x_1(k+1) = x_1(k) + hx_2(k) \\ x_2(k+1) = x_2(k) + hw \end{cases}, w = -\begin{cases} r\mathrm{sign}(a), & |a| > d \\ r\dfrac{a}{d}, & |a| \le d \end{cases} a = \begin{cases} x_2(k) + \dfrac{\sqrt{d_2 + 8r|y|} - d}{2}\mathrm{sign}(y), & |y| > hd \\ x_2(k) + \dfrac{y}{h}, & |y| \le hd \end{cases}, \begin{cases} y = x_1(k) - v(k) + hx_2(k) \\ d = rh \end{cases} \tag{35}$$

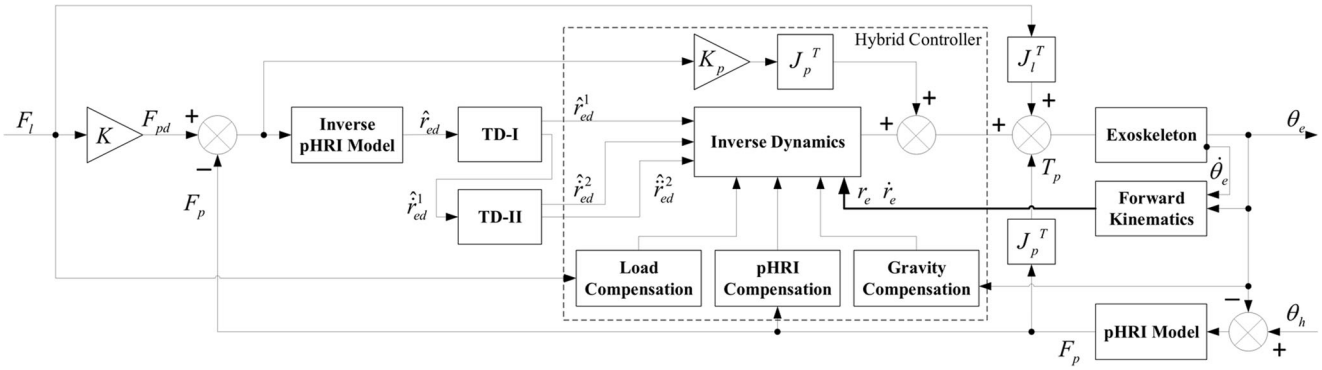

Fig. 8 Dynamic model-based control block of the LCE

where, v is the input; x_1 and x_2 are the outputs tracking v and $\dot{v}$, respectively; r and h are adjustable parameters.

Based on the multi-body exoskeleton model, the hybrid controller can be designed as:

$$\begin{aligned}\boldsymbol{\tau}_{ar} &= \boldsymbol{A}(\boldsymbol{q})\boldsymbol{u} + \boldsymbol{B}(\boldsymbol{q},\dot{\boldsymbol{q}})\dot{\boldsymbol{r}}_{\boldsymbol{e}} \\ &\quad + \boldsymbol{G}_{\boldsymbol{r}}(\boldsymbol{q}) - \boldsymbol{J}_{\boldsymbol{l}}{}^{T}(\boldsymbol{q})\boldsymbol{F}_{\boldsymbol{l}} - \boldsymbol{J}_{\boldsymbol{p}}{}^{T}(\boldsymbol{q})\boldsymbol{F}_{\boldsymbol{p}} - \boldsymbol{w} \\ &\quad + \boldsymbol{J}_{\boldsymbol{p}}{}^{T}(\boldsymbol{q})\boldsymbol{K}_{\boldsymbol{p}}\Delta\boldsymbol{F} \end{aligned} \tag{36}$$

$$\boldsymbol{u} = \ddot{\boldsymbol{r}}_{\boldsymbol{ed}} + \boldsymbol{K}_{\mathbf{1}}(\boldsymbol{r}_{\boldsymbol{ed}} - \boldsymbol{r}_{\boldsymbol{e}}) + \boldsymbol{K}_{\mathbf{2}}\left(\dot{\boldsymbol{r}}_{\boldsymbol{ed}} - \dot{\boldsymbol{r}}_{\boldsymbol{e}}\right) \tag{37}$$

where, $\boldsymbol{K}_{\mathbf{1}}$ and $\boldsymbol{K}_{\mathbf{2}}$ are positive definite diagonal matrices. Note that the differential term $\dot{\boldsymbol{r}}_{\boldsymbol{ed}}$ can be estimated by the TD-I and TD-II. For more accuracy, it can be replaced by $\Delta\boldsymbol{F}$ in Eq. (28). Then, the control law $\boldsymbol{u}$ can be modified as:

$$\boldsymbol{u} = \ddot{\boldsymbol{r}}_{\boldsymbol{ed}} + \boldsymbol{K}_{\mathbf{1}}(\boldsymbol{r}_{\boldsymbol{ed}} - \boldsymbol{r}_{\boldsymbol{e}}) + \boldsymbol{K}_{\mathbf{2}}\Delta\boldsymbol{F} \tag{38}$$

Thus, the controller can be defined by Eqs. (26), (28), (35), (36), and (38). Substituting the controller into the system dynamics Eq. (25):

$$\begin{aligned}&\Delta\ddot{\boldsymbol{r}} + \left[\boldsymbol{K}_{\mathbf{2}} + b_p\boldsymbol{A}^{-1}(\boldsymbol{q})\boldsymbol{J}_{\boldsymbol{p}}{}^{T}(\boldsymbol{q})\boldsymbol{K}_{\boldsymbol{p}}\right]\Delta\dot{\boldsymbol{r}} \\ &\quad + \left[\boldsymbol{K}_{\mathbf{1}} + k_p\boldsymbol{A}^{-1}(\boldsymbol{q})\boldsymbol{J}_{\boldsymbol{p}}{}^{T}(\boldsymbol{q})\boldsymbol{K}_{\boldsymbol{p}}\right]\Delta\boldsymbol{r} \\ &\quad = \boldsymbol{0}\end{aligned} \tag{39}$$

The multivariable time-varying system can be described with a state equation:

$$\dot{\boldsymbol{X}} = \boldsymbol{H}(\boldsymbol{q})\boldsymbol{X} \tag{40}$$

$$\boldsymbol{H}(\boldsymbol{q}) = \begin{bmatrix} \boldsymbol{0} & \boldsymbol{I} \\ \boldsymbol{K}_{\mathbf{1}} + k_p\boldsymbol{A}^{-1}(\boldsymbol{q})\boldsymbol{J}_{\boldsymbol{p}}{}^{T}(\boldsymbol{q})\boldsymbol{K}_{\boldsymbol{p}} & -\boldsymbol{K}_{\mathbf{2}} - b_p\boldsymbol{A}^{-1}(\boldsymbol{q})\boldsymbol{J}_{\boldsymbol{p}}{}^{T}(\boldsymbol{q})\boldsymbol{K}_{\boldsymbol{p}} \end{bmatrix} \tag{41}$$

For the convergence of Eq. (39), the necessary and sufficient condition is that the real parts of all eigenvalues of matrix $\boldsymbol{H}(\boldsymbol{q})$ are negative. Therefore, the designed controller is convergent, when suitable parameters $\boldsymbol{K}_{\mathbf{1}}$, $\boldsymbol{K}_{\mathbf{2}}$, and $\boldsymbol{K}_{\boldsymbol{p}}$ ae selected.

Table 4 Parameters of the exoskeleton

Limb	Length (m)	Mass (kg)	Center of mass (m)	Inertia (kg•m^2)
RF, LF	0.52	0.8	0	0.022
RS, LS	0.65	2.4	0.384	0.087
RT, LT	0.62	2.0	0.356	0.052
Torso	0.40	4.6	0.062	0.002

4 LCE Simulation

The LCE structure was built in SolidWorks, and imported into OpenSim, a biomimetic dynamics software package [42]. Table 4 lists the parameter settings of the LCE in Fig. 7. Our LCE controller was realized using MATLAB scripts, for there is an interface between OpenSim and MATLAB.

In addition to the LCE model, a human model *Gait2354* in OpenSim was introduced to provide motion guides for the LCE. The human model weighs 75.16 kg, while the LCE weighs 15 kg. The mass of the load was set to 30 kg. Note that the load mass is not modelled in the exoskeleton dynamics; instead, the forces and torque $\boldsymbol{T}_{\boldsymbol{l}}$ that the load block imposes on the exoskeleton are regarded as the load. For simplicity, the interaction between the load block and the exoskeleton was simulated by a spring damping model with stiffness coefficient $\boldsymbol{k}_{\boldsymbol{l}}$ = [10000500001000] and damping coefficient $\boldsymbol{b}_{\boldsymbol{l}}$ = [50005000100]. In addition, a gait between standing and normal walking was added to the human model [43]. The period of the gait is 1.2 s. During the simulation, only movements in the sagittal plane were considered. It is assumed that the walking process has no bipedal support period, and the swinging leg does not collide with the ground. Finally, the exoskeleton footplates were always set parallel with the ground.

First, the scale factor $\boldsymbol{K}$ is set to zero to simulate the force tracking effect of the proposed hybrid controller, in contrast to a direct force controller:

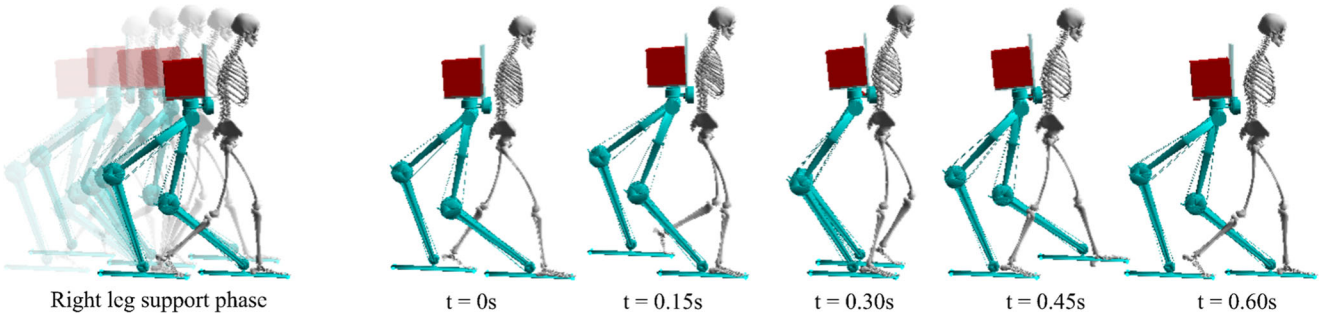

Fig. 9 A right leg support phase during the 10s walking simulation with hybrid control. Note: The phase lasts from 5.5 s to 6.1 s; the motion of the left leg support phase is virtually the same as that of the right leg

$$\tau_{ar} = J_p{}^T(q)K_{pf}F_p - D\dot{q}_r + G_r(q) - J_l{}^T(q)F_l + w \quad (42)$$

where, $K_{pf} = diag\ (5,\ 5,\ 5)$ is the proportional term coefficient; $D = diag\ (4,\ 4,\ 4)$ is a regulator of system dynamic features. The hybrid controller parameters in Eqs. (36) and (37) are selected as $K_1 = diag\ (10000,\ 10000,\ 500)$, $K_2 = diag\ (1000,\ 1000,\ 50)$, and $K_p = diag\ (3,\ 3,\ 3)$. Figure 9 shows the progress of the human-robot system walking with hybrid control. The HRI forces F_p are illustrated in Fig. 10. The results show that, compared to no-control situation, both direct force control and hybrid control converged the HRI forces to a small value near zero. However, during the standing phase in the first 2 s in Fig. 10(a), direct force control had a greater steady state error ($\Delta F_{px} = -0.3$N, $\Delta F_{py} = -8.4$N, and $\Delta T_{pz} = -2.5$Nm) than hybrid control ($\Delta F_{px} =$

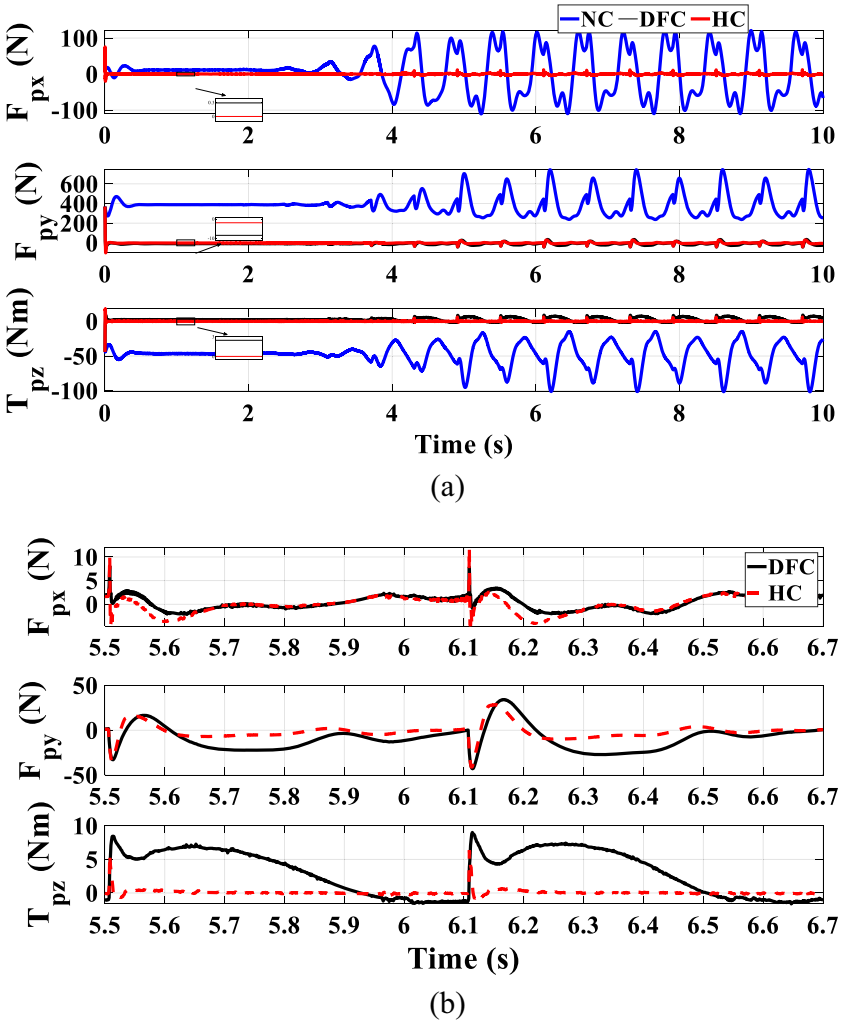

Fig. 10 Interaction forces from human to robot in no-control (NC) situation, DFC, and hybrid control (HC) (a), and interaction forces from robot to human in DFC and HC in a period of normal gait walking (b)

0.0N, ΔF_{py} = 1.9N, and ΔT_{pz} = 0.0Nm). As shown in Fig. 10(b), the hybrid control exhibited better dynamic behavior and converged faster than the direct force control during the walking phase, especially with freedom of F_{py} and T_{pz}. The peak forces are attributable to the swinging of the supporting leg, for the system does not consider human compliant landing.

Different scale factors $\boldsymbol{K}$ were selected to verify the effect of SFC. Eq. (34) shows that the wearer's efforts is positively proportional to the scale factor. Since the forward HRI force F_{px} is relatively small, this direction was set as zero force control. Therefore, three simulations were carried out with scale factor $\boldsymbol{K}$ = *diag* (0, 0.1, 0.1), $\boldsymbol{K}$ = *diag* (0, 0.2, 0.2), and $\boldsymbol{K}$ = *diag* (0, 0.5, 0.5), respectively. The results are displayed in Figs. 11 and 12.

Figure 11(a) presents the interaction force $\boldsymbol{F_l}$ between exoskeleton and backpack, where $\boldsymbol{F_l}$ can be regarded as the abovementioned load. Although the load mass was fixed at 30 kg, the load force $\boldsymbol{F_l}$ varied with the dynamic motions of the system. But the load force did not change significantly with the scale factors. Figure 11(b) presents the interaction force $\boldsymbol{F_p}$, which represents the wearer's effort. Another simulation with $\boldsymbol{K}$ = *diag* (1.0, 1.0, 1.0) was performed for comparison. Note that scale factor $\boldsymbol{K}$ = *diag* (1.0, 1.0, 1.0) is not equal to that in NC situation, where the pilot needs to carry the exoskeleton as well. The results obviously exhibited a layered effect.

Figure 12 reports the practical output scale factors. As shown in Fig. 12(a), during the standing phase, practical output scale factors k_y and k_z continuously tracked the desired setting with results $[k_y \ k_z] = [0.093 \quad 0.099]$, [0.1930.199], and [0.4930.499], respectively. However, there was some fluctuation when walking forward, especially for k_y. The period 5.5–5.6 s, a right leg supporting phase, is zoomed in Fig. 12(b). Significant oscillations were observed during the switch of supporting leg. Approximately 0.1 s and 0.05 s were required to converge, respectively. This can be effectively handled by human compliant landing. But the mechanism of human motion control, which is not yet mature, is not involved in this research.

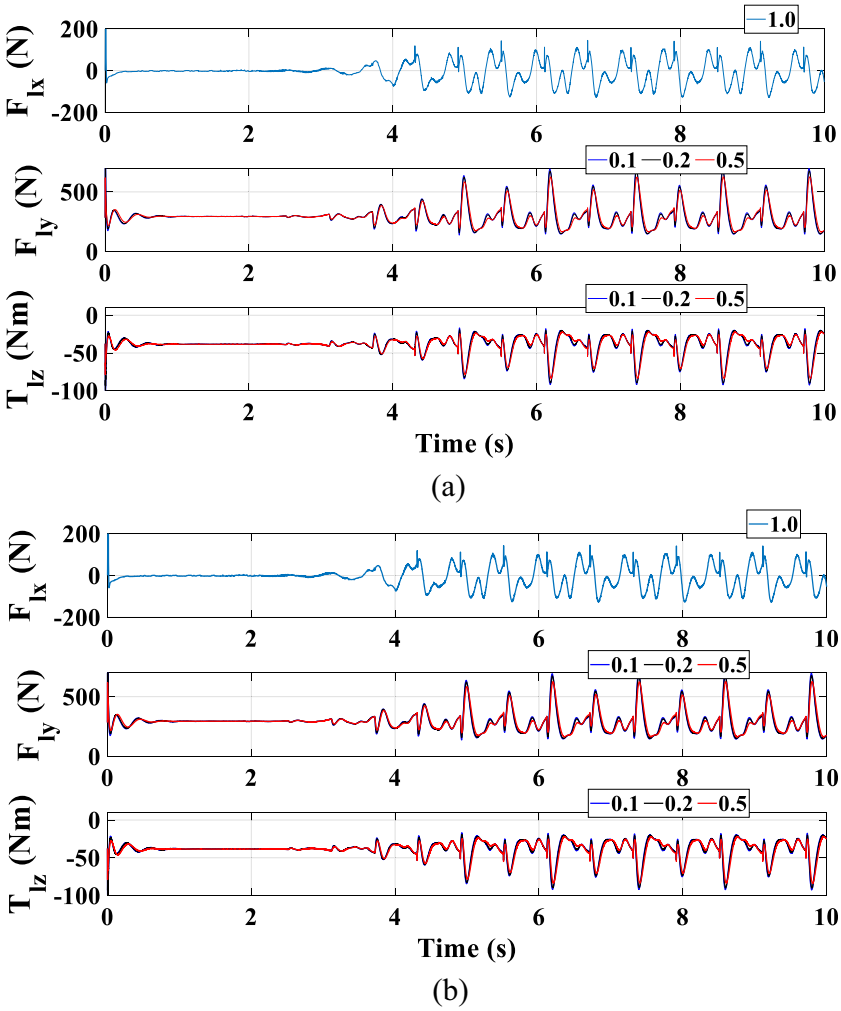

Fig. 11 Interaction forces from robot to load with different scale factors (a), and interaction forces from robot to human with different scale factors (b)

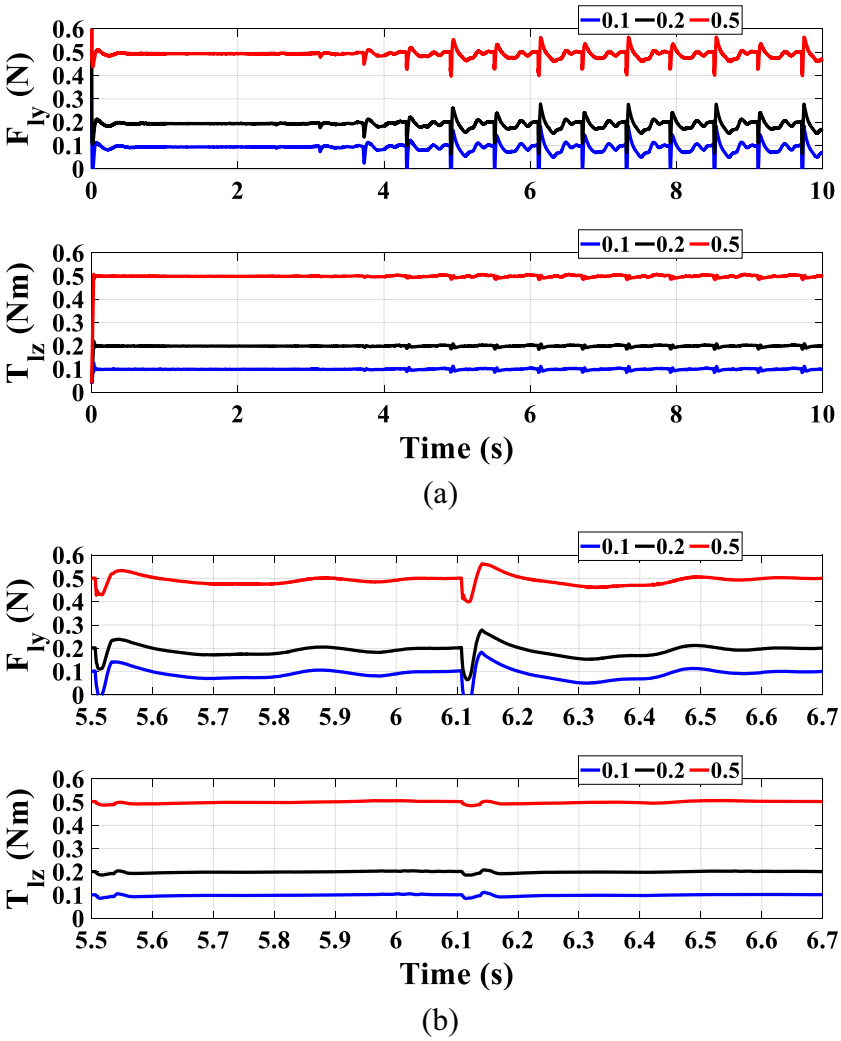

Fig. 12 Practical output scale factors during the complete progression from standing to walking (a), and those of the walking period during 5.5–6.7 s (b)

5 Conclusions

This paper examines the essential features of augmentation exoskeletons, and divided augmentation exoskeletons into two categories: HRAE and RBAE. Then, a novel mid-level control strategy called SFC was proposed to realize the simultaneous transformation of pHRI and cHRI in the human-robot coupled system. The basic idea of the SFC is that: the load is modeled separately from the robot; the pHRI force/torque is controlled in a scaled-down form. Since a lower limb exoskeleton is mainly used to carry loads, the authors built a loose-coupled load-carrying RBAE in the co-simulation environment of MATLAB and OpenSim to verify the effectiveness of SFC. Despite its compactness and ease of operation, the SFC increases the design burden of the low-level controller. Thus, direct force control and inverse dynamic control were combined to develop a hybrid low-level controller, aiming to support the mid-level control. Through an experiment on an elbow joint exoskeleton, the SFC was proved feasible, and capable of achieving the specified scale factor. The simulation results on the LCE also indicate that the SFC can be applied in complex systems. The scale factor can be set arbitrarily between 0 and 1. The smaller the scale factor, the less effort the wearer expends. If the scale factor is zero, the control is the same as zero force control. If the scale factor is greater than 1, the augmentation exoskeleton changes into an impedance trainer.

There are also some remaining issues. First, in most cases, the load force/torque in the SFC is not constant, but influenced by system states and controller type. Further research is necessary to guarantee that the exoskeleton controller design not only benefits the pilot, but also prevents the load from excessive shaking. Second, during the LCE control, the overly ideal spring damping model was adopted as the pHRI model. This calls for further work on model identification or model replacement. The future research needs to design a more robust low-level control algorithm, filter and process interaction force more effectively, probe into HBAE control, and implement actual lower limb exoskeletons.

Authors' Contributions

Lin Lang: Coding and writing
Junhao Xiao: Coding and writing
Yunshu Sun: English writing
Huimin Lu: Review and editing
Zongtan Zhou: Investigation, as well as review and editing
Chunbaixue Yang: Review and editing

Funding This work was supported by the National Natural Science Foundation of China (Grant number: 61903131 and 71904047) (Lin Lang, Chunbaixue Yang), and China Postdoctoral Science Foundation (Grant number: 2020 M683715) (Lin Lang).

Code or Data Availability The code is available from the corresponding author on reasonable request.

Declarations

Ethics Approval Not applicable

Consent to Participate The authors consent to participate in this work.

Consent for Publication The authors consent to publish this work.

Conflict of Interest The authors declare that they have no conflicts of interest to report regarding the present study.

References

1. Tucker MR, Olivier J, Pagel Aet al. Control strategies for active lower extremity prosthetics and orthotics: a review. J Neuroeng Rehabiln 2015; **12**(1): 1
2. Rupal, B.S., Rafique, S., Singla, A., et al.: Lower-limb exoskeletons: research trends and regulatory guidelines in medical and non-medical applications. Int. J. Adv. Robot. Syst. **14**(6), 1729881417743554 (2017)
3. Herr, H.: Exoskeletons and orthoses: classification, design challenges and future directions. J Neuroeng Rehabil. **6**(1), 21 (2009)
4. Gilbert K and Callan P. Hardiman i prototype. General Electric Company, Schenectady, NY, GE Tech Rep S-68-1081 1968
5. Raab, K., Krakow, K., Tripp, F., Jung, M.: Effects of training with the rewalk exoskeleton on quality of life in incomplete spinal cord injury: a single case study. Spinal Cord Series Cases. **2**, 15025 (2016)
6. Tsukahara, A., Hasegawa, Y., Eguchi, K., Sankai, Y.: Restoration of gait for spinal cord injury patients using hal with intention estimator for preferable swing speed. IEEE Trans Neural Syst Rehabil Eng. **23**(2), 308–318 (2014)
7. Baunsgaard, C.B., Nissen, U.V., Brust, A.K., et al.: Gait training after spinal cord injury: safety, feasibility and gait function following 8 weeks of training with the exoskeletons from ekso bionics. Spinal Cord. **56**(2), 106–116 (2018)
8. Zoss, A.B., Kazerooni, H., Chu, A.: Biomechanical design of the Berkeley lower extremity exoskeleton (bleex). IEEE/ASME Trans Mech. **11**(2), 128–138 (2006)
9. Yang, Z., Gu, W.: Zhang J Et al. Springer, Force control theory and method of human load carrying exoskeleton suit (2017)
10. Fontana, M., Vertechy, R., Marcheschi, S., Salsedo, F., Bergamasco, M.: The body extender: a full-body exoskeleton for the transport and handling of heavy loads. IEEE Robotics Auto Magaz. **21**(4), 34–44 (2014)
11. Cornwall W. In Pursuit of the Perfect Power Suit, 2015
12. Dollar, A.M., Herr, H.: Lower extremity exoskeletons and active orthoses: challenges and state-of-the-art. IEEE Trans. Robot. **24**(1), 144–158 (2008)
13. Pons, J.L.: Wearable Robots: Biomechatronic Exoskeletons. John Wiley & Sons (2008)
14. Lee, H.D., Lee, B.K., Kim, W.S., Han, J.S., Shin, K.S., Han, C.S.: Human–robot cooperation control based on a dynamic model of an upper limb exoskeleton for human power amplification. Mechatronics. **24**(2), 168–176 (2014)
15. Hong, M.B., Shin, Y.J., Wang, J.H.: Novel three-DOF ankle mechanism for lower-limb exoskeleton: kinematic analysis and design of passive-type ankle module. IEEE/RSJ Int Conf Intell Robots Syst. 504–509 (2014)
16. Kim, J., Shin, M., Ahn, D.H., Son, B.J., Kim, S., Kim, D.Y., et al.: Design of a knee exoskeleton using foot pressure and knee torque sensors. Int J Adv Robot Syst. **12**(2), 101–112 (2015)
17. Walsh, C.J., Endo, K., Herr, H.: A quasipassive leg exoskeleton for load-carrying augmentation. Int J Human Robot. **4**, 487–506 (2007)
18. Walsh, C.J., Paluska, D., Pasch, K., Grand, W., Valiente, A., Herr, H.: Development of a lightweight, underactuated exoskeleton for load-carrying augmentation. IEEE Int Conf Robot Autom. 3485–3491 (2006)
19. Kim, H., Seo, C., Shin, Y.J., Kim, J., Kang, Y.S.: Locomotion control strategy of hydraulic lower extremity exoskeleton robot. IEEE Int Conf Advanc Intell Mechatron. 577–582 (2015)
20. Lee, H., Lee, B., Kim, W., Han, J.: Human-robot cooperation control based on a dynamic model of an upper limb exoskeleton for human power amplification. Mechatronics. **24**, 168–176 (2014)
21. Hussain, S., Xie, S.Q., Jamwal, P.K.: Adaptive impedance control of a robotic orthosis for gait rehabilitation. IEEE Trans Syst Man Cybern Part B Cybern. **43**, 1025–1034 (2013)
22. Koopman, B., Van Asseldonk, E.H.F., Van Der, K.H.: Selective control of gait subtasks in robotic gait training: foot clearance support in stroke survivors with a powered exoskeleton. J Neuroeng Rehabil. **10**, 1–10 (2013)
23. Al-Shuka HF and Song R. On low-level control strategies of lower extremity exoskeletons with power augmentation. In *2018 Tenth International Conference on Advanced Computational Intelligence (ICACI)*. IEEE, pp. 63–68
24. Chen, S., Chen, Z., Yao, B., Zhu, X., Zhu, S., Wang, Q., Song, Y.: Adaptive robust cascade force control of 1-dof hydraulic exoskeleton for human performance augmentation. IEEE/ASME Trans Mechatronics. **22**(2), 589–600 (2016)
25. Chen, S., Chen, Z., Yao, B.: Precision cascade force control of multi-dof hydraulic leg exoskeleton. IEEE Access. **6**, 8574–8583 (2018)
26. Li, Z., Su, C.Y., Wang, L., Chen, Z., Chai, T.: Nonlinear disturbance observerbased control design for a robotic exoskeleton incorporating fuzzy approximation. IEEE Trans. Ind. Electron. **62**(9), 5763–5775 (2015)
27. Lee, S., Sankai, Y.: Virtual impedance adjustment in unconstrained motion for an exoskeletal robot assisting the lower limb. Adv. Robot. **19**(7), 773–795 (2005)
28. Yang Z, Zhu Y, Yang X et al. Impedance control of exoskeleton suit based on adaptive rbf neural network. In *2009 International Conference on Intelligent Human-Machine Systems and Cybernetics*, volume 1. IEEE, pp. 182–187
29. Tran, H.T., Cheng, H., Rui, H., Lin, X.C., Duong, M.K., Chen, Q.M.: Evaluation of a fuzzy-based impedance control strategy on a powered lower exoskeleton. Int. J. Soc. Robot. **8**(1), 103–123 (2016)
30. Aguirre-Ollinger G, Colgate JE, Peshkin MA et al. Activeimpedance control of a lower-limb assistive exoskeleton. In *2007 IEEE 10th international conference on rehabilitation robotics*. IEEE, pp. 188–195

31. Lenzi, T., Carrozza, M.C., Agrawal, S.K.: Powered hip exoskeletons can reduce the user's hip and ankle muscle activations during walking. IEEE Trans Neural Syst Rehab Eng. **21**(6), 938–948 (2013)
32. Boaventura T, Hammer L and Buchli J. Interaction force estimation for transparency control on wearable robots using a kalman filter. In *Converging clinical and engineering research on neurorehabilitation II*. Springer, 2017. pp. 489–493
33. Masud, N., Smith, C., Isaksson, M.: Disturbance observer based dynamic load torque compensator for assistive exoskeletons. Mechatronics. **54**, 78–93 (2018)
34. Brahmi, B., Saad, M., Lam, J.T.A.T., Luna, C.O., Archambault, P.S., Rahman, M.H.: Adaptive control of a 7-dof exoskeleton robot with uncertainties on kinematics and dynamics. Eur. J. Control. **42**, 77–87 (2018)
35. Ka, D.M., Hong, C., Toan, T.H., Qiu, J.: Minimizing humanexoskeleton interaction force by using global fast sliding mode control. Int. J. Control. Autom. Syst. **14**(4), 1064–1073 (2016)
36. Mao, Y., Jin, X., Dutta, G.G., et al.: Human movement training with a cable driven arm exoskeleton (carex). IEEE Trans Neural Syst Rehabil Eng. **23**(1), 84–92 (2014)
37. Beil J, Perner G and Asfour T. Design and control of the lower limb exoskeleton kit-exo-1. In *2015 IEEE International Conference on Rehabilitation Robotics (ICORR)*. IEEE, pp. 119–124
38. Perry, J.C., Rosen, J., Burns, S.: Upper-limb powered exoskeleton design. IEEE/ASME Trans Mechatron. **12**(4), 408–417 (2007)
39. Rocon E, Ruiz A, Raya R et al. Human-robot physical interaction. *Wearable Robots*: Biomechatronic Exoskeletons 2008: 127–163
40. Schiele, A., van der Helm, F.C.: Influence of attachment pressure and kinematic configuration on phri with wearable robots. Appl Bionics Biomech. **6**(2), 157–173 (2009)
41. Jinqing, H., Lulin, Y.: The discrete form of tracking differentiator. J Syst Sci Math Sci. **3**, (1999)
42. Seth, A., Hicks, J.L., Uchida, T.K., Habib, A., Dembia, C.L., Dunne, J.J., Ong, C.F., DeMers, M.S., Rajagopal, A., Millard, M., Hamner, S.R., Arnold, E.M., Yong, J.R., Lakshmikanth, S.K., Sherman, M.A., Ku, J.P., Delp, S.L.: Opensim: simulating musculoskeletal dynamics and neuromuscular control to study human and animal movement. PLoS Comput. Biol. **14**(7), e1006223 (2018)
43. Anderson, F.C., Pandy, M.G.: Dynamic optimization of human walking. J. Biomech. Eng. **123**(5), 381–390 (2001)

Lin Lang received the B.S. degree, M.S. degree, and Ph.D. degree from National University of Defense Technology(NUDT) in 2006, 2009, and 2016 respectively. From 2018, he is a lecturer in Hunan University of Finance and Economics. His research interests include legged robot control, nonlinear control theory.

Junhao Xiao (M′12-SM′19) received his Ph.D. (2013) from Department of Informatics, University of Hamburg, Hamburg, Germany, and his B.E. degree (2007) from the National University of Defense Technology, Changsha, China. In 2013, he joined the Department of Automatic Control, National University of Defense Technology, Changsha, China. From 2017, he serves as an associate professor on Robotics and Cybernetics. The focus of his research lies on mobile robotics, especially on localization, mapping, path planning, human-robot interaction and muti-robot coordination. In these areas, he has published over 50 peer-reviewed journal and conference papers as author or co-author. He has served as an executive committee member for RoboCup Middle Size League from 2017 to 2019.

Yunshu Sun received a bachelor′s degree from Shenyang University of technology in 2004. In 2014, she served as a senior engineer of CNNC Liaoning Nuclear Power Co., Ltd., mainly engaged in the design and procurement of electrical instrument and control equipment.

Huimin Lu (S′09-M′11) received his Bachelors of Engineering (2003), Masters of Engineering (2005) and Ph.D. (2010) from the National University of Defense Technology (NUDT), Changsha, China. Later, he joined the Department of Automatic Control, NUDT (2010) where he is now an full professor on robotics and cybernetics. From 2014 to 2015, he was a visiting scholar at the University of Tuebingen, Germany. The focus of his research is on mobile robotics, mainly on robot vision, path planning, multi-robot coordination, robot soccer and robot rescue. In these areas, he has published over 80 peer-reviewed journal and conference papers as author or co-author.

Zongtan Zhou received his Bachelors of Engineering (1990), Masters of Engineering (1994) and and Ph.D. (1998) from National University of Defense Technology (NUDT), China. He was promoted to Professor in 2007. His research interests include brain–computer interface, cognitive neuroscience, image/signal processing, computer/biological vision, and neural networks.

Chunbaixue Yang received the B.S. degree, M.S. degree, and Ph.D. degree from Central South University (CSU) in 2008, 2011, and 2018 respectively. From 2021, she is an associate professor in Hunan University of Finance and Economics. Her research interests include technological innovation, innovation network, and knowledge management.